N·H

ELSEVIER

Monte Carlo simulation of 0.1–100 keV electron and positron transport in solids using optical data and partial wave methods

J.M. Fernández-Varea [a,b], D. Liljequist [b,*], S. Csillag [b], R. Räty [b], F. Salvat [a]

[a] Facultat de Física (ECM), Universitat de Barcelona, Diagonal 647, 08028 Barcelona, Spain
[b] Fysikum, University of Stockholm, Box 6730, S-113 85 Stockholm, Sweden

Abstract

A new Monte Carlo code for the detailed simulation of the transport of low-energy electrons and positrons in solids is presented, including a critical discussion of concepts and approximations in the scattering model. Inelastic scattering is calculated using a Bethe surface model based on optical and photoelectric data for the solid, making possible a good accuracy at low energies, and a high resolution (~ 1 eV) in simulated energy loss spectra. Exchange corrections for electrons and relativistic corrections for energies up to ~ 100 keV are included. Elastic scattering is calculated by means of a differential cross section obtained by relativistic partial wave analysis for an exchange-corrected muffin-tin Dirac–Hartree–Slater atomic potential. In the simulation, no adjustments of parameters to empirical scattering data are made. For comparison, measurements have been made of the characteristic low energy loss spectrum of 100 keV electrons through a thin silicon film. Simulated results for electrons and positrons are also compared with other available experimental data, in particular at low (a few keV) energies. In general, very good agreement is obtained.

1. Introduction

Since more than three decades, the method of Monte Carlo simulation has been used to calculate the scattering and energy loss of charged particles penetrating matter [1]. The introduction of this method to the scattering of low-energy electrons (at kinetic energies ~ 10 keV) [2,3] has stimulated the practical application of successively more accurate elastic and inelastic single scattering differential cross sections (e.g. Refs. [4–12]), as well as simple models combined with empirical corrections (e.g. Refs. [13–15]). More recently, there has been an increasing interest in the calculation of low-energy positron scattering (see e.g. Ref. [16]), and improved cross section models have been introduced in particular for the inelastic scattering of low-energy electrons and positrons (see e.g. Refs. [17–19]).

Our intention with this work has been to construct a Monte Carlo code applicable to electrons or positrons with energies down to ~ 100 eV, and, moreover, useful for simulating energy loss distributions with high accuracy, e.g. showing the effects of the characteristic loss spectrum at a ~ 1 eV resolution. Simple relativistic corrections are added to make the code applicable up to ~ 100 keV. The code is named LEEPS (low energy electron and positron simulation).

At the relatively low energies thus considered, we may neglect bremsstrahlung as a source of energy loss. On the other hand, the energies are high enough that we also shall be able to disregard electron–phonon or positron–phonon interaction. Methods for the simulation of such interaction, important at energies below ~ 10 eV, have recently been described by Akkerman et al. [20]. Thus we have to consider only elastic scattering, i.e. the deflection of the incident particle in the screened Coulomb field of the nuclei, and the energy loss caused by single or collective electron excitation in the solid.

For the elastic scattering we have used relativistic partial wave analysis of the scattering against a static atomic potential, which is nowadays a well-known, near-standard method in this context (see e.g. Ref. [8]). By means of this method, which appears to be useful for elastic scattering in solids down to kinetic energies ~ 100 eV, it seems that much of the difference between positron and electron transport may be well understood. Questions remain as regards the validity of this method at lower energies when applied to scattering in solids. For the inelastic scattering we have used a model based on optical and photoelectric data for the scattering solid; this, in fact, is what makes possible the accuracy in simulating energy loss distributions. Optical data have previously been implemented in Monte Carlo simulations by Jensen and Walker [16], by Öztürk and Williamson [21], and – in a more approximate manner and with a fur-

---

* Corresponding author. E-mail cemd@vana.physto.se.

ther empirical adjustment to scattering data – by Ding and Shimizu [22]. Our model differs from the approach used by these authors in various respects; in particular, it allows the introduction of exchange and relativistic corrections in a simple and natural way, and LEEPS is thus equally well suited for the simulation of electron and positron transport.

In subsequent sections, we first describe the physical model in LEEPS. We examine concepts, assumptions and approximations, but avoid computational details. We then outline the simulation procedure. Detailed derivations and the complete description of sampling procedures are given in a separate report [23]. For brevity and clearness, equations are here written without the exchange corrections or relativistic corrections which are included in LEEPS. These corrections are briefly indicated in Appendix A, and are fully described in Refs. [23,24].

Finally we compare results of LEEPS with experiment, in particular with regard to results at lower energies and at high energy loss resolution, and also with regard to the differences between electron and positron transport. Partly we have compared with a measurement on our JEOL-100C electron microscope, partly with experimental data reported in the literature.

2. Elastic scattering

2.1. General aspects

In electron or positron scattering with energy loss in not too thin solid layers, one may usually disregard effects due to the coherent scattering from many atoms, i.e. diffraction and channeling effects. Under these conditions the elastic scattering process may be treated as a succession of independent (incoherent) scattering events along a particle trajectory, each event consisting of the particle (= incident electron or positron) being scattered in the potential field $V(r)$ of a single, as-if isolated atom. The incoherent scattering may be seen as due to a change of the electron or positron wavelength because of energy loss (inelastic scattering), and to disorder in the structure of the scattering material. It should be noted, however, that the grain size in polycrystalline materials is typically large compared to the elastic or inelastic mean free path for electrons or positrons in the keV energy region. Also, it is well known that diffraction patterns (albeit diffuse) are obtained also for scattering in amorphous materials. This suggest that it is basically the presence of energy loss, i.e. some minimum amount of inelastic scattering, which is required to make calculations based on the trajectory picture generally adequate.

The reliability of the single-atom model should however be questioned when the particle wavelength is of the order of the interatomic distances or larger, which occurs at kinetic energies below ∼ 50 eV. At these energies it may accordingly be questioned if the initial and final states of the particle are well described as free-particle states. Moreover, the static field approximation may be invalid (i.e. charge polarization of the target atom may become important). Thus, we do not expect our elastic scattering calculation to be reliable below ∼100 eV.

The solid is assumed to consist of one element only, with atomic number Z. The single-atom scattering potential $V(r)$ is not expected to be the potential $V_f(r)$ of a free atom; rather, it should be modified by the presence of neighbour atoms, i.e. by the local crystalline or amorphous structure. With a random direction of motion relative to this structure, it is however reasonable to assume a spherically symmetric average scattering potential $V(r)$. As a consequence, the angular distribution from a single-scattering event is axially symmetric, i.e. independent of the azimuthal scattering angle.

With these various approximations, the elastic scattering is simply described in terms of a differential cross section (DCS) per atom, which may be written as $d\sigma_{el}/d\theta$, where θ is the polar scattering angle. Moreover, it is implicitly assumed that the solid is homogeneous and isotropic on a scale of the order of the average distance between scattering events. The probability for the particle to travel a distance s without being elastically scattered is then $\exp(-s/\lambda_{el})$, where λ_{el} is the elastic mean free path, given by $\lambda_{el} = (N\sigma_{el})^{-1}$, N is the number of atoms per unit volume and σ_{el} the total elastic cross section per atom.

This constitutes the well-known conventional model, used also in LEEPS, for particle trajectories due to incoherent plural or multiple elastic scattering in solids. Since the number of collisions on a typical low- or medium-energy trajectory is not too large, individual collisions may be simulated directly. The well-known multiple scattering approaches due to Goudsmit and Saunderson [25], Lewis [26] and Molière [27] are not useful in the low-energy region. (See e.g. Ref. [28] for a recent discussion.)

2.2. Scattering potential in condensed matter

Since the use of a single-atom scattering potential is itself an approximation, the proper choice or calculation of $V(r)$ may be not quite trivial. The solid-state modification $V_f(r) \rightarrow V(r)$ has been considered, e.g. by Green and Leckey [4], Valkealahti and Nieminen [9], Liljequist et al. [29] and Czyzewski et al. [30]. We avoid entering a detailed discussion here, but merely give qualitative arguments to support the model presently adopted [8,31]. These are: 1) the gradient $dV(r)/dr$ should be closely equal to $dV_f(r)/dr$ for small r, 2) by symmetry, $dV(r)/dr$ should vanish midway to an (average) nearest-neighbour atom, 3) the gauge should be chosen so that $V(r) = 0$ beyond this distance, and 4) to lowest order, $V(r)$ might be estimated by simple superposition of contributions $V_f(r)$ from the central and close neighbour atoms.

These requirements are satisfied by a simple "muffin-tin model" [8,31]

$$V(r) = \begin{cases} V_{\mathrm{f}}(r) + V_{\mathrm{f}}(2r_{\mathrm{mt}} - r) - 2V_{\mathrm{f}}(r_{\mathrm{mt}}), & \text{if } r < r_{\mathrm{mt}}, \\ 0, & \text{if } r > r_{\mathrm{mt}}. \end{cases}$$

$$(1)$$

Here, r_{mt} is the muffin-tin radius. The value of this radius is, in principle, an adjustable parameter, but a physically reasonable choice is to put r_{mt} equal to the radius r_{WS} of the Wigner–Seitz sphere, i.e. essentially taking an average of half the distance to the neighbouring lattice points. A slightly different choice would be, for example, to take r_{mt} equal to half the nearest-neighbour distance. A similar, more detailed construction of $V(r)$ is that given in Ref. [9]. Another method, based on applying spherical Wigner–Seitz boundary conditions to the calculation of atomic wave functions, is used for example in Ref. [29].

The effect of the solid-state modification of the scattering potential (i.e. using $V(r)$ rather than $V_{\mathrm{f}}(r)$) may be substantial on the scattering at small angles and on the *total* elastic mean free path λ_{el}. However, the effect on the scattering at medium or large angles is in general small. This is easily understood qualitatively, since such scattering classically corresponds to trajectories near the nucleus. The effect on plural or multiple scattering, which is conveniently measured in terms of the transport mean free path $\lambda_{\mathrm{tr}} = \lambda_{\mathrm{el}}/(1 - \langle \cos\theta \rangle)$, is therefore rather small [29]. This may be regarded as a fortunate circumstance, which makes possible the use of rather simple approximations to account for the solid-state modification of the atomic scattering field.

For the present code, the muffin-tin potential (1) with $r_{\mathrm{mt}} = r_{\mathrm{WS}}$ has been applied, using parameterized and tabulated free-atom potentials $V_{\mathrm{f}}(r)$ which have been calculated by the Dirac–Hartree–Slater method and fitted to a sum of Yukawa-type potentials [32]. An additional correction in the case of elastic scattering of electrons is made by adding a local exchange potential (see e.g. Ref. [33]).

2.3. Elastic cross section calculation

With the single-atom scattering potential $V(r)$ defined, the next problem is to choose the appropriate method for computing the elastic cross section. The simplest method is the Born approximation, which is valid provided that $v/c \gg Z/137$, where v is the velocity of the incident particle and c the velocity of light in vacuum. This may be written

$$E \gg \tfrac{1}{2}(Z/137)^2 mc^2, \tag{2}$$

where E is the non-relativistic kinetic energy of the particle. The right member of the inequality is, for example, 85 keV for gold, 9 keV for iron and 0.2 keV for beryllium. At energies of these orders of magnitude or smaller, the Born approximation is not reliable.

For some time, partial wave analysis (PWA) has therefore been used for the calculation of the elastic DCS used in Monte Carlo simulations at lower energies. It is common to use PWA based on the Dirac equation ("relativistic" or Dirac

PWA) (see e.g. Refs. [6,34,35]) rather than PWA based on the Schrödinger equation [9,11]. Relativistic effects (kinematic effects but also the effects of the spin of the incident electron or positron) are then systematically included. DCSs are typically obtained as numerical tables, from which desired values are obtained by interpolation; this is not a significant disadvantage with presently available computers.

The difference between electron and positron elastic scattering at low energies is mainly due to that the scattering occurs in a non-coulombic potential (namely, the screened Coulomb field of the nucleus). In this potential it turns out that an electron is scattered to a somewhat larger extent than a positron of the same energy, resulting primarily in a shorter transport mean free path [36]. A qualitative explanation is that the electron, being negatively charged, tends to move closer to the nucleus than the positron and therefore experiences a stronger deflecting field. This difference is of course not obtained in the Born approximation, and it does not arise in a non-relativistic (Schrödinger equation) treatment of scattering in a pure Coulomb field. A further difference between electron and positron elastic scattering arises when the Dirac equation is used. This difference is due essentially to the presence of spin-orbit interaction in the Dirac PWA, which increases with the velocity of the incident electron or positron. It is therefore small at low energies, but becomes dominant at high energies. It should be noted, however, that at low energies both effects, although certainly not negligible, are small compared to the considerable error caused by the Born approximation. A quantitative comparison is given in Refs. [29,36].

The elastic DCSs used in LEEPS are computed with Dirac PWA. The computational method has been described in detail by Salvat and Mayol [33].

3. Inelastic scattering

3.1. General aspects

In the early simulations (e.g. Ref. [3]), and in some more recent (e.g. Ref. [6]), the energy loss is often calculated in the continuous-slowing-down approximation. The energy loss on a short path length segment Δs is then taken to be equal to $(-dE/ds)\Delta s$, where $-dE/ds$ is the stopping power, i.e. the average energy loss per unit path length. This may lead to erroneous results, since straggling is neglected – i.e. the fact that energy is actually lost in discrete collisions. The number of such collisions fluctuates statistically on a given path length and the energy loss W in each collision varies in accordance with a probability distribution corresponding to the inelastic DCS. In fact, straggling is considerable in electron or positron penetration through matter, largely due to that the incident particle occasionally suffers a large fractional energy loss W/E in a close collision with an atomic electron (or, at highly relativistic energies, in a radiative collision). As is well known, however,

the continuous-slowing-down approximation is often accurate enough for the computation of e.g. transmission and backscattering fractions in thin films, while it fails badly as regards for example the energy distribution of transmitted particles. Analytic approaches such as the Landau [37] and Vavilov [38] distributions, which give formulae for the energy distribution after a given path length segment Δs, are valid only in the limit of multiple inelastic scattering, i.e. primarily at high energies. A detailed simulation of the energy loss process is therefore necessary in order to obtain generally accurate results and realistic energy loss distributions at low and intermediate energies.

The inelastic DCS is conveniently counted per atom. Again we assume that all azimuthal scattering angles in a single inelastic collision are equally probable. The inelastic DCS may then be written as $d^2\sigma_{in}/(d\theta dW)$, where θ is the polar scattering angle. This is integrated over θ and W to give the total inelastic cross section σ_{in}. If the solid may be considered as isotropic and homogeneous as regards the probability of an inelastic event, the probability for no inelastic event during a path length s is $\exp(-s/\lambda_{in})$, where the inelastic mean free path $\lambda_{in} = (N\sigma_{in})^{-1}$ is introduced.

Most inelastic scattering events in a solid – the excitation of single electrons in the conduction or valence bands and collective excitations – cannot be physically associated with a particular atom. Formally, however, they may be regarded as contributing to the atomic cross section. For example, if the mean free path for plasmon excitation is λ_p, then the contribution to the atomic inelastic cross section may consistently be taken to be $\sigma_p = (N\lambda_p)^{-1}$.

A single inelastic scattering event is conveniently described in terms of the variables Q and W (rather than θ and W), i.e. by a DCS $d^2\sigma_{in}/(dQdW)$. Here, Q is an energy which is a measure of the momentum change of the electron or positron in the collision. In the non-relativistic case

$$Q = \frac{(p_i - p_f)^2}{2m}, \tag{3}$$

where p_i and p_f are the initial and final electron (or positron) momenta. If the incident particle collides with a free target electron initially at rest, the momentum transfer $p_i - p_f$ is equal to the momentum of the target electron after the collision, from which follows that $Q = W$ in this case. This motivates the short name "recoil energy" for Q.

The kinetic energy E of the incident particle, the energy loss W, the recoil energy Q and the polar scattering angle θ in an inelastic scattering event are related by the kinematic formula

$$\frac{Q}{E} = 2 - \frac{W}{E} - 2\sqrt{1 - W/E}\cos\theta. \tag{4}$$

The extreme angles $\theta = 0°$ and $\theta = 180°$ determine the upper limit of possible W for a given Q, which gives

$$W_{max} = 2\sqrt{EQ} - Q. \tag{5}$$

This defines the integration domain when calculating for example total inelastic cross section, stopping power and energy loss probability distributions. Alternatively, this domain may be defined by the minimum and maximum Q obtained from Eq. (4) for a given $W < W_{max}$.

The calculation of the inelastic DCS may start either from the Bethe theory for the inelastic scattering of fast electrons from free atoms [39,40], or from the dielectric theory for the energy loss of charged particles in condensed matter [41,42] [1]. Both theories are essentially first-order, i.e. valid within the Born approximation. Strictly speaking, the condition for the general validity of the Born approximation in this context may be written $v \gg u_K$, where u_K is the orbital velocity of the atomic (target) K-shell electrons [40]. (In the non-relativistic case, this condition may actually also be written as Eq. (2).) This makes both theories at least partially invalid at energies below a limit larger than the K-shell binding energy B_K. The use of these theories at lower energies may however be heuristically justified as follows. The atomic inelastic DCS can be *approximately* regarded as a sum of independent contributions from subshells for which $E > B_i$, where B_i is the binding energy of subshell i [44]. The contribution to the inelastic cross section from such a subshell is roughly proportional to B_i^{-1}. For independent contributions from subshells such that $E \gg B_i$ the validity condition (2) may reasonably be assumed satisfied. Consequently, the error in the Born approximation inelastic DCS is expected to be small, except at energies E near or below the smallest B_i. In the case of condensed matter, this should be interpreted as an energy of the order of the plasmon energy corresponding to the density of valence electrons.

In the Bethe theory, the inelastic DCS per atom may be written [40]

$$\frac{d^2\sigma}{dQdW} = \frac{\pi e^4}{E} \frac{1}{WQ} \frac{df(Q,W)}{dW}, \tag{6}$$

where $df(Q,W)/dW$ is the generalized oscillator strength (GOS) density (per unit energy transfer W). The GOS density is essentially a map of all possible atomic transitions in the Born approximation, and thus contains all the information about the atom that is required for the calculation of the cross section [40]. As motivated by the classical theory of absorption and dispersion [45], the quantity $(df(Q,W)/dW)\,dW$ may be regarded as the number of electrons per atom that take part in inelastic excitations with recoil energy Q and energy transfer between W and $W+dW$. In agreement with this view, the quantum mechanical Bethe sum rule

$$\int_0^\infty \frac{df(Q,W)}{dW}\,dW = Z \tag{7}$$

---

[1] A quite different method is represented by binary encounter models, such as the widely and sometimes uncritically used inner-shell excitation theory of Gryzinski [43].

is obeyed for any Q. In the limit $Q \rightarrow 0$ the GOS becomes equal to the optical oscillator strength (OOS) density $df(0, W)/dW \equiv df(W)/dW$ which describes the excitation of a free atom by photons in the dipole approximation.

If the atom is initially in the ground state (which we assume), the GOS is a non-negative function, known as the Bethe surface [40], which is defined on the (Q, W) plane. Excitations to continuum levels form a continuous part of the Bethe surface. In particular one may note the so-called Bethe ridge [40] along the line $W = Q$, which corresponds to close, approximately binary collisions between the incident particle and an atomic electron, with an energy transfer much larger than the binding energy.

In the dielectric theory, the inelastic DCS per atom may be written [41]

$$\frac{d^2\sigma}{dQ dW} = \frac{\pi e^4}{E}\frac{1}{WQ}\frac{2W}{\pi\Omega_p^2} Z \, \mathrm{Im}\left(\frac{-1}{\epsilon(Q, W)}\right), \qquad (8)$$

where Ω_p is the fictitious plasmon energy of a free-electron gas with a density equal to the total average electron density in the condensed matter, i.e.

$$\Omega_p = (4\pi\hbar^2 e^2 NZ/m)^{1/2}. \qquad (9)$$

The quantity which plays a role analogous to the Bethe surface is the "energy loss function" $\mathrm{Im}(-1/\epsilon(Q, W))$, where $\epsilon(Q, W)$ or equivalently $\epsilon(K, \omega)$ is the dielectric constant of the condensed matter as a function of the electromagnetic field wavevector K and frequency ω. Here, $Q = \hbar^2 K^2/2m$ and $W = \hbar\omega$, i.e. a quantized interaction is understood. The dielectric constant describes polarization as well as energy absorption in matter exposed to electric (electromagnetic) fields [45]; thus, inelastic scattering is connected to the optical properties of the solid.

The two cross sections are trivially identical if we put

$$\frac{df(Q, W)}{dW} = \frac{2W}{\pi\Omega_p^2} Z \, \mathrm{Im}\left(\frac{-1}{\epsilon(Q, W)}\right). \qquad (10)$$

It should be noted that this relation actually alters and extends the GOS density concept so as to make it include also those effects which are associated with the polarization of the scattering medium by the incident charge, i.e., screening of the charge and collective excitations. These effects are not explicitly part of the Bethe theory, which deals with the excitation of a single atom exposed to the unscreened field of an incident particle. The OOS density which describes the excitation of the atom by photons is related to the dielectric constant by [46]

$$\frac{df(W)}{dW} = \frac{2W}{\pi\Omega_p^2} Z \, \mathrm{Im}\left(\epsilon(W)\right). \qquad (11)$$

(This is also easily shown by starting from ϵ written as a sum of contributions from Lorentz oscillators.) Eq. (11) is evidently not equal to the limit of the modified GOS, Eq. (10), when $Q \rightarrow 0$. A simple, intuitive insight into the physical content of Eq. (10) is to note that in order to reach Eq. (10) from Eq. (11), we have to replace $\mathrm{Im}(\epsilon)$ by

$$\mathrm{Im}(-1/\epsilon) = \frac{\mathrm{Im}(\epsilon)}{|\epsilon|^2}. \qquad (12)$$

The factor $|\epsilon|^2$ in the denominator may be regarded as a measure of the screening of the incident charge. When $|\epsilon|^2 = 1$, for example in a thin gas, the dielectric theory reduces to the Bethe theory. Screening is also negligible at frequencies $\omega = W/\hbar$ corresponding to the excitation of inner shells.

With this in mind, it is clear that we can use the formalism of the Bethe theory also for inelastic scattering in condensed matter; we shall speak, for example, of the Bethe surface of a free-electron gas. (Assuming the gas to be a model of the conduction or valence electrons, we may either count the GOS per atom, in which case Eq. (7) is valid, or the GOS per electron, in which case the Bethe sum rule adds to unity.) The Bethe surface thus defined for condensed matter includes collective excitations, evidenced in the maxima of $\mathrm{Im}(-1/\epsilon(Q, W))$. As is usual, we shall refer to the optical limit ($Q \rightarrow 0$) of the condensed matter GOS as the "OOS", although it is the same function as in the case of free atoms only in the limit $|\epsilon| \rightarrow 1$.

3.2. Bethe surface model

As is evident from Eq. (6), the Bethe surface $df(Q, W)/dW$, together with the kinematic restrictions (4) and (5), determines the inelastic DCS. Rather than modelling the physical scattering process (as for example in the binary encounter theories [43]), we may look for a model of the Bethe surface.

We use here a simple and flexible method, convenient for Monte Carlo simulation, namely to build a model of the Bethe surface as a sum (or integral) of contributions of the general form $f(Q)\delta(W - W_r(Q))$, where δ is the Dirac δ-function, $f(Q)$ a Q-dependent oscillator strength, and $W_r(Q)$ a relation connecting each momentum transfer with a specific energy transfer [19,47] [2]. In the limit $Q \rightarrow 0$ it is natural to regard W_r as a resonance energy, connected to an oscillator resonance frequency $\omega = W_r/\hbar$. In fact, any Bethe surface can be constructed by a suitable, specific choice of such δ-function contributions [47]. However, it should be stressed that we do not attempt to reconstruct the exact Bethe surface, but only to build a physically reasonable model of it.

We may write the Bethe surface as [19]

$$\frac{df(Q, W)}{dW} = \left[\frac{df(Q, W)}{dW}\right]_i + \left[\frac{df(Q, W)}{dW}\right]_v, \qquad (13)$$

where the subscript "i" indicates the contribution from inner-shell ionization (excitation to states above the Fermi level),

---

[2] This method has been used several times previously [10,18,19,47]. We give here a condensed description.

while "v" indicates the contribution from the excitation of weakly bound (valence) electrons.

For the "i" contribution we use the model [19,48]

$$\left[\frac{df(Q,W)}{dW}\right]_i = \int \left[\frac{df(W')}{dW'}\right]_i F_\delta(W';Q,W)\, dW',$$

(14)

where $[df(W')/dW']_i$ is the OOS for inner-shell excitation, and where

$$F_\delta(W';Q,W) = \delta(W-W')\Theta(W'-Q)$$
$$+\delta(W-Q)\Theta(Q-W').$$

(15)

(Here, Θ is the step function, i.e. $\Theta(x) = 0$ if $x < 0$ and $\Theta(x) = 1$ if $x > 0$.) The first term in Eq. (15) (non-zero for $Q < W'$) is a model of optically allowed (dipole) excitations. These may be regarded as resonance excitations of the atom in the fluctuating electric field of a charged particle passing by at some distance [49]. The second term (non-zero for $Q > W'$) is a model of optically forbidden excitations, i.e. the classically close, binary collisions which produce the Bethe ridge. The Bethe ridge is in Eq. (15) modelled as $\delta(W-Q)$, i.e. the width of the ridge due to the orbital motion of the atomic electron is neglected. (This approximation is discussed below.) The total oscillator strength obtained by integrating Eq. (15) from $W = 0$ to $W = \infty$ is unity for all Q. The expression (15) is therefore referred to as a "unit-strength (or one-electron) δ-oscillator" [10,19]. The OOS density of the δ-oscillator consists of a single peak $\delta(W-W')$ at the resonance energy W'. Although extremely simple, the δ-oscillator model has been shown to be useful for approximately calculating inner-shell (core electron) excitation [48,50–52]. According to a study by Bichsel [53], it may be better than the Gryzinski model [43] for this purpose.

For the contribution "v" to the Bethe surface from valence-electron excitation we use the model [19]

$$\left[\frac{df(Q,W)}{dW}\right]_v = \int \left[\frac{df(W')}{dW'}\right]_v F_{TM}(W';Q,W)\, dW',$$

(16)

where $[df(W')/dW']_v$ is the OOS for excitation of weakly bound electrons, and where

$$F_{TM}(W';Q,W) = f_p(Q)\,\delta(W-W_p(Q))$$
$$+(1-f_p(Q))\,\delta(W-Q)$$

(17)

is the so-called two-modes (TM) model [11,19]. This model approximates the Lindhard theory [54] of the free-electron gas. The first term in Eq. (17) represents the plasmon contribution with plasmon damping (i.e. finite plasmon linewidth) neglected. The function $f_p(Q)$ is a Q-dependent plasmon oscillator strength and $W_p(Q)$ is the plasmon dispersion relation. The recoil energy Q is here connected

to the plasmon wavevector k by $Q = \hbar^2 k^2/2m$. The plasmon energy in the limit of infinite wavelength ($k \to 0$) is $W' = W_p(0)$. The oscillator strength $f_p(Q)$ is (counted per electron in the gas) equal to unity at $Q = 0$, then drops with increasing Q, and vanishes for $Q \geq Q_c$, where Q_c is the recoil energy corresponding to the plasmon cut-off (maximum) wavevector k_c. The second term in Eq. (17) is a model of the electron-hole excitations, where the incident charged particle through a binary collision knocks a target electron out of the Fermi sphere. The momentum distribution of the electrons in the gas is ignored, so that $Q = W$, i.e. the Bethe ridge is again contracted into a δ-function. In order to satisfy the Bethe sum rule, the oscillator strength must be $1 - f_p(Q)$ in the second term. This represents the screening of the binary interaction at low momentum transfer (i.e. at long distances), due to collective displacement of the gas. As may be seen from Eq. (17), there are two modes (two branches) for $Q < Q_c$; hence the name of the model. The OOS density is a single peak $\delta(W-W')$.

Since the Bethe sum rule adds to unity when applied to Eq. (17), we refer also to the TM model as a unit-strength or one-electron oscillator, with the resonance energy W' in the $Q = 0$ limit. With appropriate expressions for $f_p(Q)$ and $W_p(Q)$ [19], it reproduces nearly exactly the results of the Lindhard theory as regards inelastic mean free path and stopping power for electrons or positrons penetrating the free-electron gas.

In the lowest approximation, a single δ-oscillator (Eq. (15)), multiplied by an appropriate oscillator strength f_i, may be used as a model for all excitations of electrons belonging to a particular inner subshell i [48,52]. In order to perform a more accurate simulation of energy loss distributions, the possible excitations of the electrons in each subshell i (including the valence electrons) may be modelled by a large number of such oscillators with different strengths $f_{i,j}$ distributed over resonance energies $W'_{i,j}$, $j = 1, 2, 3, \ldots$ This method was implemented in a previous code [10]. A very simple improvement would evidently be to use the TM model for the valence electrons.

The present approach is however different in several respects, one of them being that the set of discrete oscillators is replaced by a continuum, as explicitly shown in Eqs. (14) and (16); this is in practice a prerequisite for the simulation of energy loss distributions at high resolution.

3.3. Application of optical data

It may be noted that main contributions to the inelastic DCS are obtained at small Q values, i.e. most inelastic collisions occur with a small scattering angle θ. (Small momentum transfers are classically associated with large impact parameters, and therefore also with large cross sections.) A Taylor expansion of the Bethe theory expression for $d\sigma_{in}/dW$ for energy losses $W \ll E$ at small scattering angles gives [19]

$$
\left[\frac{d\sigma_{in}}{dW}\right]_{\theta<\theta_{max}} = \int_{Q(\theta=0)}^{Q(\theta=\theta_{max})} \frac{d^2\sigma_{in}}{dQdW}\, dQ
$$

$$
\approx \frac{\pi e^4}{E}\frac{1}{W}\frac{df(W)}{dW}\ln\left[1+\left(\frac{2E\theta_{max}}{W}\right)^2\right].
$$

(18)

Thus, in order to compute the inelastic DCS in an approximation which is good enough to reproduce the characteristic low energy loss spectrum, as well as a good estimate of the total inelastic cross section [44], we need only to know the OOS density. This is not sufficient for the calculation of energy loss during penetration of matter, since the small-angle DCS in Eq. (18) represents only part of the stopping power. However, Eq. (18) is a key to understand the potential accuracy of optical-data models.

Penn [17] applied the idea of using an experimentally determined OOS density, obtained from the measurement of optical properties of the scattering solid, for the calculation of inelastic scattering. In this way, one may, as seen from Eq. (18), be fairly certain that the characteristic energy loss spectrum and the inelastic mean free path are obtained with good accuracy. The use of optical data was previously discussed by Ritchie and Howie [55], and optical data have extensively been used for the computation of inelastic mean free path and stopping power by Ashley [18,56–58].

In order to obtain a model for the complete inelastic scattering process, we need also a physically reasonable algorithm for extending the OOS to the $Q > 0$ region; i.e. to a Bethe surface. Penn [17] used the Lindhard [54] expression for the dielectric constant of the free-electron gas, in close analogy with the local plasma approximation [59]. Ashley [18,56–58] has employed a δ-function representation of the free-electron gas which is simpler and somewhat less accurate than the TM model, namely (in the present notation)

$$
F_A(W';Q,W) = \delta(W-(W'+Q)).
$$

(19)

A comparative discussion is given in Ref. [47].

The algorithm used in the present Monte Carlo code is based on the Bethe surface model described above (Eqs. (13)–(17)). However, a drawback of optical-data models is that the experimental OOS itself is not unambiguously separated into contributions from different bands or shells; this causes difficulties also, for example, when calculating the secondary electron yield. As an approximation, we therefore introduce a parameter W_s, which serves to divide the OOS into two parts, one due to weakly bound electron excitation and the other to inner-shell electron excitation. The Bethe surface used in LEEPS is given by [19]

$$
\frac{df(Q,W)}{dW} = \int_0^\infty \left[\frac{df(W')}{dW'}\right]_{exp} F(W';Q,W)\, dW',
$$

(20)

where

$$
F(W';Q,W) = F_{TM}(W';Q,W)\,\Theta(W_s-W')
$$
$$
+F_\delta(W';Q,W)\,\Theta(W'-W_s).
$$

(21)

Here, $\left[df(W')/dW'\right]_{exp}$ is the experimental OOS density, regarded as a continuous function of the resonance energy W', and obtained from tabulated optical and photoelectric data [60–64]. The $F(W';Q,W)$ is a unit-strength δ-function contribution to the Bethe surface, weighted with the oscillator strength density $df(W')/dW'$, and taken to be a TM model oscillator for $W' < W_s$, and a δ-oscillator for $W' > W_s$.

We suggest that W_s should be chosen to be equal to the smallest inner-shell excitation threshold energy [19]. The OOS density for sufficiently small W' is due entirely to the excitation of weakly bound (valence) electrons, and it is reasonable to expect that the TM oscillator should be better than the δ-oscillator in this region. For higher W', the energy loss spectrum shows an edge structure which is due to the excitation of inner shells, and in order to reproduce this structure for $Q \neq 0$ the δ-oscillator model should be used [47]. However, it must be noted that for $W' > W_s$ there is also a continuous background due to the excitation of valence electrons, e.g. the tail of a damped plasmon.

Applying the formula (6) for the inelastic DCS, we get

$$
\frac{d^2\sigma}{dQdW}
$$

$$
= \frac{\pi e^4}{E}\frac{1}{WQ}\int_0^\infty \left[\frac{df(W')}{dW'}\right]_{exp} F(W';Q,W)\, dW'
$$

$$
= \int_0^{W_s} \left[\frac{df(W')}{dW'}\right]_{exp}\frac{\pi e^4}{E}\frac{1}{WQ}F_{TM}(W';Q,W)\, dW'
$$

$$
+ \int_{W_s}^\infty \left[\frac{df(W')}{dW'}\right]_{exp}\frac{\pi e^4}{E}\frac{1}{WQ}F_\delta(W';Q,W)\, dW'
$$

$$
\equiv \int_0^{W_s} \left[\frac{df(W')}{dW'}\right]_{exp}\frac{d^2\sigma_{TM}}{dQdW}\, dW'
$$

$$
+ \int_{W_s}^\infty \left[\frac{df(W')}{dW'}\right]_{exp}\frac{d^2\sigma_\delta}{dQdW}\, dW',
$$

(22)

where the last member defines the *one-electron* DCSs for the TM oscillator and the δ-oscillator, i.e. $d^2\sigma_{TM}/(dQdW)$ and $d^2\sigma_\delta/(dQdW)$, respectively [19]. The point of practical importance here is that the contributions from these one-electron DCSs to the inelastic mean free path and the stopping power can be expressed by closed formulae [23]. The specific properties of the particular solid enter only in the experimental OOS density.

It has been shown [19] that the present optical-data model gives inelastic mean free paths and stopping powers in good agreement with available experimental data. The method for preparing the optical data (i.e. the OOS) is briefly indicated in Appendix B and described in Ref. [19].

We may note the following as compared with previous Monte Carlo models. Since the TM model closely reproduces the Lindhard theory, the Penn model [17] is approximately obtained by choosing $W_s = \infty$ in Eq. (22). In their Monte Carlo code, Jensen and Walker [16] apply the Penn model to the inelastic scattering. The comparative advantage with the TM model is that it lends itself more easily than the full Lindhard theory to exchange and relativistic corrections. Thus, our code is useful for simulation of electron as well as positron transport. Moreover, it may have a practical advantage when applied to Monte Carlo simulation [23]. Another difference from the code by Jensen and Walker is that we use a different extension (the δ-oscillator) for the core electrons. In partial agreement with this, Öztürk and Williamson [21] use dielectric theory and optical data only for the weakly bound electrons. For the inner-shell excitation they apply, as is the most common procedure, the Gryzinski model [43]. As mentioned, we believe that the δ-oscillator used together with optical or photoelectric data may be better than the Gryzinski model for the core electrons. The Monte Carlo code of Valkealahti and Nieminen [9] uses the Gryzinski model for both valence-electron and inner-shell excitations, which is a method analogous to the use of only δ-oscillators [10].

The shape of the atomic Bethe ridge was discussed by Inokuti for the case of hydrogen [40]. In the present model (and also in the original Bethe theory for the stopping power) the Bethe ridge is approximated as $\delta(W - Q)$, i.e. the target electron in a close collision is assumed to be initially free and at rest. This approximation is in general sufficiently accurate for simulating energy loss distributions, as may also be guessed from the fact that it is actually made in the derivation of the Landau [37] and Vavilov [38] distributions. It also allows the introduction of exchange and relativistic corrections in a simple and straightforward manner (see Appendix A). The approximation may turn out to be insufficient, if for example electron Compton scattering (i.e. the target electron momentum distribution) is studied [65]. Ding and Shimizu [66] and Ashley [18,56–58] have used Eq. (19) to extend the OOS into the GOS, and in so doing they attribute a certain width to the Bethe ridge. However, the effect of their procedure is simply that the OOS, shifted to higher energies by the amount Q, is obtained if a cut is made through the Bethe surface at any Q. As regards including the width and shape of the Bethe ridge in a simulation, the Penn model, being based on the full Lindhard theory of the free-electron gas, should be more realistic, at least for the weakly bound electrons.

4. Simulation methods

4.1. General aspects

The complete picture needed for detailed trajectory simulation is in principle as follows. The DCSs, and all quantities derived from them, depend on the particle kinetic energy E. The total cross section is $\sigma = \sigma_{el} + \sigma_{in}$, and the total mean free path is $\lambda = (N\sigma)^{-1}$. The probability that a particle with a given energy E will travel a path length s without interacting with the solid is $\exp(-s/\lambda)$. In accordance with this, the path length s to the next point of interaction is sampled by $s = -\lambda \ln \xi$, where ξ is a random number between 0 and 1. The probability that the interaction will be elastic is σ_{el}/σ; otherwise it is inelastic. If the interaction is elastic, a polar scattering angle θ is sampled from the probability distribution function

$$p_{el}(\theta) = \frac{1}{\sigma_{el}} \frac{d\sigma_{el}}{d\theta}. \tag{23}$$

If the interaction is inelastic, a scattering angle θ and an energy loss W are sampled from the probability distribution function

$$p_{in}(\theta, W) = \frac{1}{\sigma_{in}} \frac{d^2\sigma_{in}}{d\theta dW}. \tag{24}$$

The energy E is then decreased by W. In both cases, a value for the azimuthal scattering angle ϕ is chosen randomly between 0 and 2π. The angles θ and ϕ together determine the new direction of motion of the particle towards the next point of interaction; and so on.

The special interpolation and sampling methods used to obtain scattering angles and energy loss in the individual scattering events in LEEPS are described in detail in Ref. [23]. Here we will only briefly indicate these methods. The tabulation of and sampling from the OOS is of particular interest, and in this case we will make an exception from our intention of not going into technical details. As regards program organization, LEEPS actually consists of a few subroutines (dealing with data preparation and with the sampling of scattering angles and energy loss in single events) which can be conveniently inserted into a user-made main program [23]. The programming language is standard FORTRAN 77.

4.2. Simulation of inelastic events

The basic idea in the simulation of an inelastic event in LEEPS is first to sample the excited oscillator (i.e. the resonance energy W'), and then to sample the recoil energy Q and the energy loss W in accordance with the corresponding one-electron DCS (TM model or δ-oscillator). The variable Q is then easily transformed to the scattering angle θ, using Eq. (4). The first step requires the OOS data for the scattering solid; the second step requires a fixed set of formulae derived for the two-modes model and the δ-oscillator.

From an initial table of OOS values $\mathrm{d}f(W')/\mathrm{d}W'$ at given resonance energies W' (see Appendix B), the OOS is evaluated by linear log–log interpolation, i.e. by linear interpolation of $\ln(\mathrm{d}f(W')/\mathrm{d}W')$ as a function of $\ln W'$.

The probability of exciting an oscillator with resonance energy in the interval $(W', W' + \mathrm{d}W')$ is given by

$$p_{\mathrm{osc}}(E; W')\,\mathrm{d}W' = \frac{\mathrm{d}f(W')}{\mathrm{d}W'} \frac{\sigma_{\mathrm{in}}(W')}{\sigma_{\mathrm{in}}}\,\mathrm{d}W', \qquad (25)$$

where $\sigma_{\mathrm{in}}(W')$ is the *one-electron* total cross section (at that particular electron or positron energy E), i.e. the cross section for exciting a unit-strength oscillator with resonance energy W'.

The normalized probability distribution function given by Eq. (25) is tabulated on a grid of resonance energies W'_j (independent of the energy of the projectile) from which $p_{\mathrm{osc}}(E; W')$ is obtained by linear log–log interpolation. Since $\sigma_{\mathrm{in}}(W')$ is a slowly varying function of W' except near E, the probability distribution function $p_{\mathrm{osc}}(E; W')$ has a shape similar to that of the OOS except for a rapid decrease at resonance energies near E due to the decrease of $\sigma_{\mathrm{in}}(W')$ when W' approaches E (see Fig. 1). Therefore, the grid of resonance energies W'_j where $p_{\mathrm{osc}}(E; W')$ is tabulated must be selected in such a way that: (i) the OOS obtained by linear log–log interpolation from a table of OOS values at the points of this grid does not differ signifi-

cantly from the input OOS and (ii) the grid is dense enough to properly reproduce the rapid decrease of $\sigma_{\mathrm{in}}(W')$ for W' values approaching E. In the simulation program we use a grid of $N_{\mathrm{r}} = 300$ resonance energies W'_j determined so as to fulfill these requirements. First, the grid of the input OOS table is "cleaned" by discarding those data points which can be obtained by interpolation between neighbouring points with an error less than a given "tolerance" (typically a few percent). This cleaning reduces the number of grid points considerably. The remaining points, say N_1, are concentrated in the regions where the OOS varies rapidly (as can be seen in Fig. 1). The grid is then completed, by linear interpolation on a log–log scale, with $N_2 = N_{\mathrm{r}} - N_1$ points at resonance energies logarithmically distributed in the interval from 0.5 eV to 500 keV. The final grid is dense enough to follow the rapid variation of $p_{\mathrm{osc}}(E; W')$ near the maximum possible W' value at a given energy E. Fig. 1 shows explicitly the tabulated values of $p_{\mathrm{osc}}(E; W')$ for 1 keV electrons in aluminium.

Before starting the simulation, the arrays $\lambda_{\mathrm{in}}^{-1}(E_i)$ and $p_{\mathrm{osc}}(E_i; W'_j)$ $(j = 1, \ldots, N_{\mathrm{r}})$ are computed and stored in the computer memory on a grid of kinetic energies E_i (which is actually the same as used in the simulation of elastic scattering). For a given kinetic energy E, such that $E_i \leq E \leq E_{i+1}$, the resonance energy W' of the excited oscillator is obtained by linear log–log interpolation, i.e. as

$$
\begin{aligned}
W'(E, \xi) = \exp\Big\{ & \ln W'(E_i, \xi) \\
& + \big[\ln W'(E_{i+1}, \xi) - \ln W'(E_i, \xi)\big] \\
& \times \frac{\ln E - \ln E_i}{\ln E_{i+1} - \ln E_i} \Big\}. \qquad (26)
\end{aligned}
$$

Exact random sampling of W' is then performed from the distribution $p_{\mathrm{osc}}(E_i; W')$ defined by linear log–log interpolation in the $p_{\mathrm{osc}}(E_i; W'_j)$ table.

Sampling of Q and W from the appropriate one-electron oscillator (δ-oscillator or TM model, depending on whether $W' > W_{\mathrm{s}}$ or $W' < W_{\mathrm{s}}$) is made from analytical formulae, by means of the rejection method combined with the inverse transform method. Details are found in Ref. [23]. The random sampling of Q and W is simplified by the fact that each one-electron oscillator can be split up into separate contributions, each represented by a single-valued dispersion relation $W = W(Q)$. This means that we may integrate the DCS over one of these variables to obtain the (unnormalized) probability distribution function of the other. A value of this other variable is sampled. The value of the first variable is then obtained from the dispersion relation.

Fig. 1. The dashed curve shows, for aluminium, a representation of the OOS density $\mathrm{d}f(W')/\mathrm{d}W'$ (in eV^{-1}). The dots are the remaining original OOS data after "cleaning", as explained in the text, with a tolerance of 5%. The dashed curve consists of straight lines between these dots, i.e. it is obtained by linear interpolation on a log–log scale. The continuous curve shows the ratio $\sigma_{\mathrm{in}}(W')/\sigma_{\mathrm{in}}$ (see Eq. (25)) for the case of 1 keV electrons. For the same case, the crosses show the tabulated values of the probability distribution function $p_{\mathrm{osc}}(E; W')$ (in eV^{-1}). The small discontinuity in $\sigma_{\mathrm{in}}(W')/\sigma_{\mathrm{in}}$, which occurs at $W' = W_{\mathrm{s}}$, is due to the switch from the TM model to the δ-oscillator.

4.3. Simulation of elastic events

For the angular deflection in elastic scattering events it is convenient to consider the DCS as a function of the variable
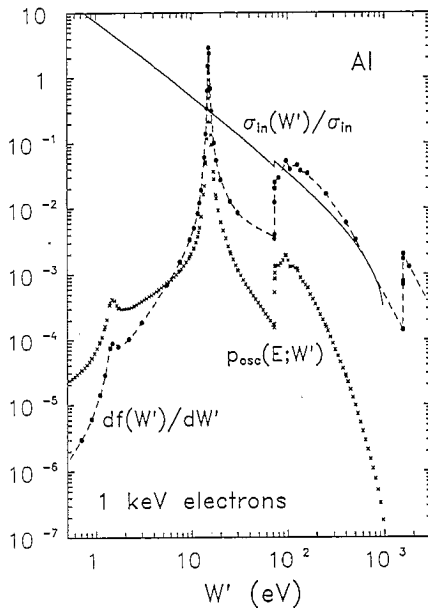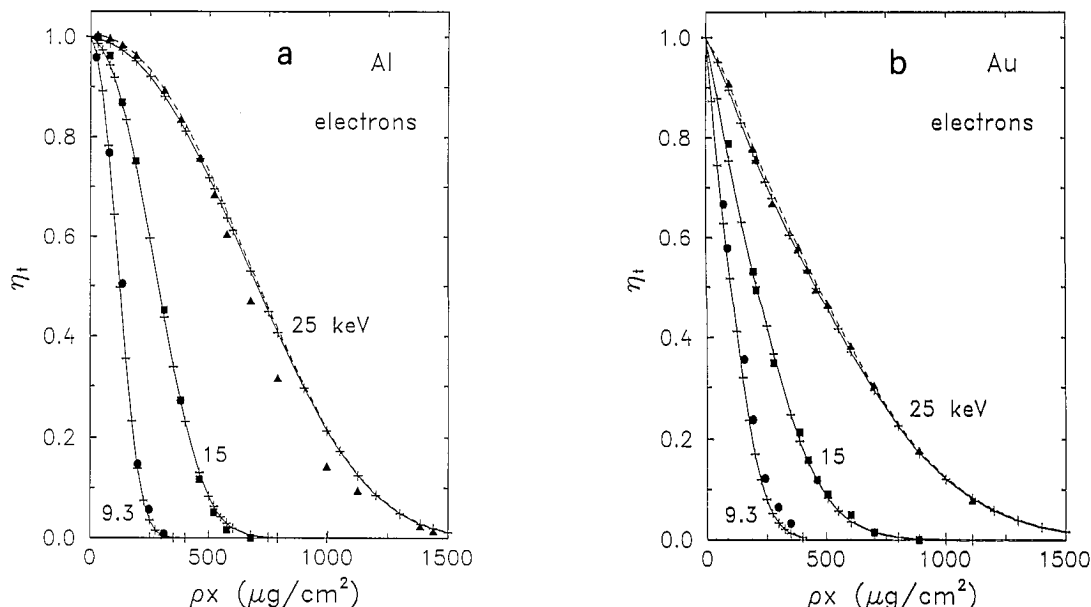
Fig. 2. Transmission fraction, η_t, for electrons with the indicated kinetic energies, through (a) aluminium and (b) gold films, as a function of mass thickness ρx. Crosses (joined by straight segments for visual aid) show LEEPS results. Experimental results are from Reimer and Drescher [67] (circles) and Neubert and Rogaschewski [68] (squares and triangles). For the case of 25 keV electrons, dashed curves show LEEPS results corrected for the contribution of energetic secondary electrons.

$$\mu \equiv \frac{1 - \cos\theta}{2}, \qquad (27)$$

which varies from 0 (forward scattering) to 1 (backward scattering). The DCS for elastic scattering of electrons or positrons with kinetic energy E can be written as

$$\frac{d\sigma}{d\mu} = \sigma_{el}\, p_{el}(E;\mu), \qquad (28)$$

where σ_{el} is the total elastic cross section and $p_{el}(E;\mu)$ is the normalized probability distribution function of the angular deflection μ in single scattering events.

During the simulation, the inverse mean free path $\lambda_{el}^{-1}(E)$ and the angular distribution $p_{el}(E;\mu)$ for the required values E and μ are obtained by linear log–log interpolation within a precomputed table, according to methods similar to those described above [23].

5. Comparison with experimental data

When comparing simulations made by LEEPS with experimental data, the following should be noted. First, there are two parameters in the present model whose values are not definitely fixed, namely the muffin-tin radius r_{mt} and the energy W_s. As described above, one can choose appropriate values by physical arguments. The experimental OOS represents of course a massive amount of empirical input, which is derived from optical and photoeffect measurements and calculations. However, no adjustments of any parameters to empirical electron or positron scattering data have

been made, and in this sense the calculation performed by LEEPS is *ab initio*.

Second, an inspection of the following features is of particular interest when comparing LEEPS results with experiment: 1) the accuracy at low energies (below 10 keV, say); 2) the ability to reproduce accurately the differences between electron and positron transport in solids; 3) the ability to simulate characteristic low energy loss spectra with high energy resolution. Present comparisons are not exhaustive, but indicate that a good accuracy may be expected.

The number of simulated tracks for each of the different cases discussed below was sufficient (at least 200 000 tracks) to make statistical uncertainties in the results insignificant as regards our present conclusions. The cutoff energy when simulating transmission and backscattering was set to 50 eV.

Figs. 2–4 compare LEEPS with some well-known benchmark electron scattering experiments. These simulations are not particularly "difficult", i.e. simpler Monte Carlo schemes may appear to give similar good agreement. However, the present results are satisfactory from the point of view that although no empirical adjustments have been made, the agreement is in general very good.

Fig. 2 shows a comparison as regards total transmission of electrons through films of different thicknesses. In Figs. 3 and 4 we consider transmitted and backscattered energy loss distributions obtained under multiple scattering conditions, at a moderate energy resolution; i.e., traces of the characteristic energy loss spectra are essentially washed out. The simulated results in Figs. 2 and 4 should be corrected for the contribution from energetic secondary electrons, which
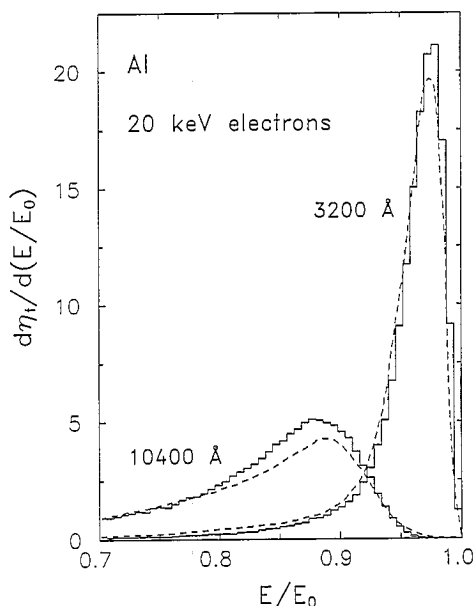
Fig. 3. Energy distributions, $d\eta_t/d(E/E_0)$, for electrons with initial energy $E_0 = 20$ keV transmitted through aluminium films. Histograms: Monte Carlo simulation by LEEPS. Dashed curves: experimental data from Shimizu et al. [5].

is discussed below.

A comparison between experimental and simulated data for the angular dependence of positron bulk backscattering from Coleman et al. [71] is shown in Fig. 5. Our simulated results are slightly (perhaps negligibly) closer to the experimental data when compared with the simulations reported
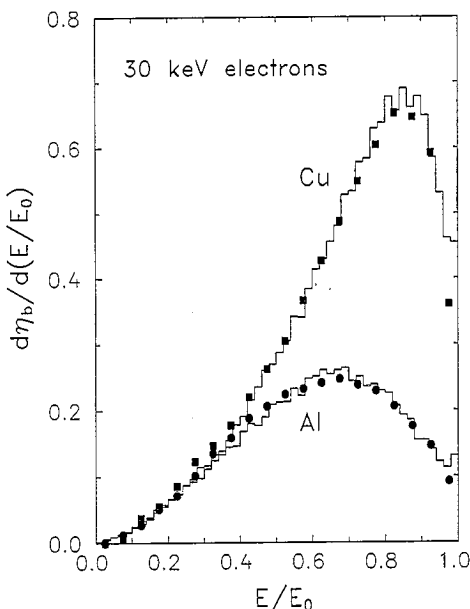
Fig. 4. Energy distributions, $d\eta_b/d(E/E_0)$, for $E_0 = 30$ keV electrons backscattered from bulk aluminium and copper. Circles and squares: experimental data from Darlington [69], normalized to the bulk-backscattering fraction as measured by Drescher et al. [70]. Histograms: Monte Carlo simulation by LEEPS.

in Ref. [71], which were made with the Jensen and Walker code [16], then claimed to be the most sophisticated model available for positron transport [71].

Fig. 6 presents a comparison with experimental data for the energy dependence of the bulk backscattering of positrons and electrons at normal incidence. Note the logarithmic energy scale. The difference between electron and positron backscattering is striking. Bulk backscattering is theoretically interesting, as it is the result of a delicate balance of elastic and inelastic scattering, as well as a balance of single large-angle and multiple scattering; i.e. essentially all parts of the scattering model seem to matter if an accurate result is to be obtained in an *ab initio* approach. In view of this, we consider the agreement between simulation and experiment in Fig. 6 to be encouraging. It should be noted that we have not included the recent experimental data on electron backscattering from Böngeler et al. [78]. At energies below a few keV, these data are in marked disagreement with simulated and experimental results shown here. In the case of positron backscattering from gold there are two sets of experimental data, namely that from Coleman et al. [71] and that from Mäkinen et al. [73]. Our results fall between these sets, but are closer to the former.

In fact, there is one correction in the case of electrons which is presently not included in LEEPS, namely the contribution to transmission and backscattering from energetic secondary electrons. By "energetic" we mean secondary electrons escaping from the solid with energies above 100 eV. This contribution has been estimated by help of another Monte Carlo program, PENELOPE [79]. Using PENELOPE, we have for the different experimental situations calculated the number of escaping energetic secondary electrons per incident primary electron. This number has been added to the transmission and backscattering fractions simulated by LEEPS, and the result is indicated by dashed curves in Figs. 2 and 6. The correction to the bulk backscattering (Fig. 6) is substantial. The correction to the transmission (Fig. 2) is found to be smaller, amounting to an increase of the transmission at a given thickness by a factor typically about 1.01–1.03. In Fig. 3, no correction is required, since the maximum secondary electron energy is half the initial electron energy. In Fig. 4, the good agreement at energies *less* than half the initial energy may be fortuitous. The experimental data from Ref. [69] agree very well with the LEEPS simulation *without* the correction for secondary electrons. However, these experimental data were normalized to the Drescher et al. [70] bulk-backscattering fraction, which thus might be slightly too low, judging from the present analysis. The missing contribution to the energy loss distributions in Fig. 4 should be mainly at the low energy part of the distributions, and actually seems to be present e.g. in the experimental results of Matsukawa et al. [80].

Fig. 7 shows a comparison with the characteristic energy loss spectrum of 100 keV electrons transmitted through a thin silicon film. An ion milled silicon wafer was analyzed using a JEOL-100C scanning transmission electron micro-
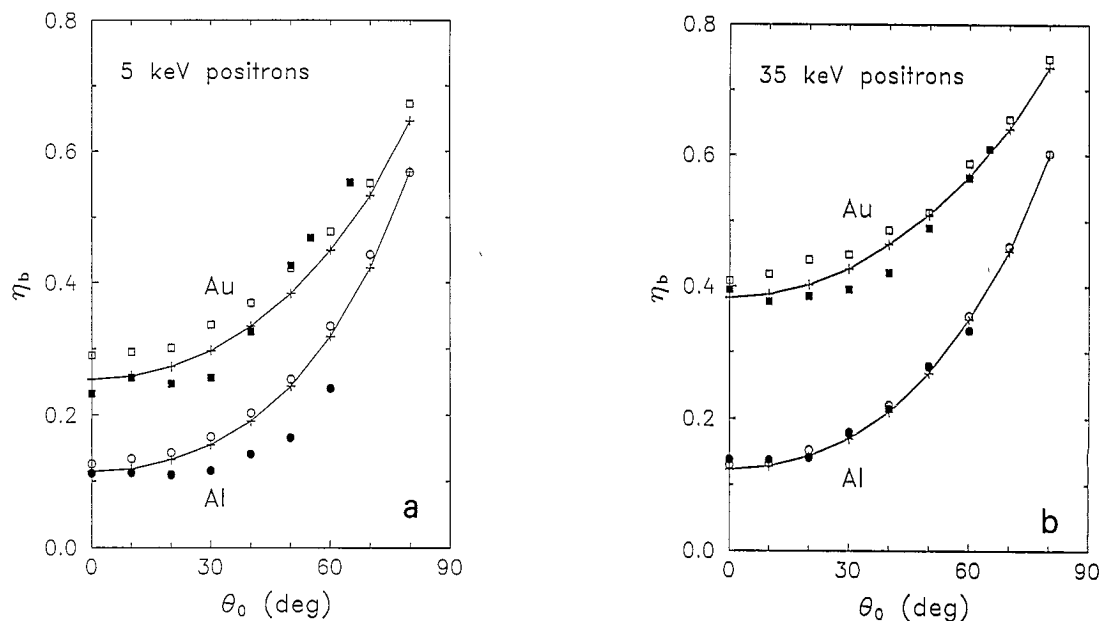
Fig. 5. Bulk-backscattering fraction, η_b, for (a) 5 keV and (b) 35 keV positrons incident on aluminium and gold, as a function of the angle of incidence θ_0. Crosses joined by straight segments show LEEPS results. Experimental (full symbols) and simulated data using the Jensen and Walker code [16] (open symbols) are taken from Coleman et al. [71].
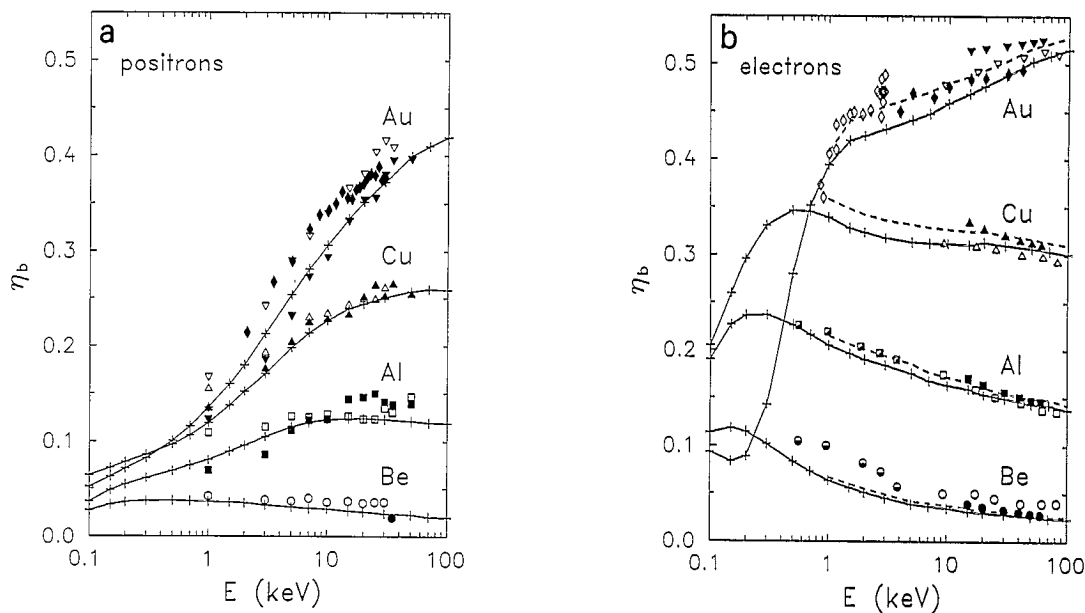

Fig. 6. Bulk-backscattering fraction for positrons and electrons normally incident on beryllium, aluminium, copper and gold, as a function of incident particle energy E. Crosses joined by straight segments show LEEPS results. Dashed curves show LEEPS results corrected for the energetic secondary electron contribution for $E \geq 1$ keV. (a) Incident positrons. Simulated data using the Jensen and Walker code [16]: ($\circ$, $\square$, $\triangle$, $\triangledown$) [71]. Experimental data: ($\bullet$) [72]; ($\blacksquare$, $\blacktriangle$, $\blacktriangledown$) [71]; ($\blacklozenge$) [73]. (b) Incident electrons. Experimental data: ($\circ$, $\square$, $\triangle$, $\triangledown$) [70]; ($\ominus$, $\blacksquare$) [74]; ($\diamond$) [75]; ($\blacklozenge$) [76]; ($\bullet$, $\blacksquare$, $\blacktriangle$, $\blacktriangledown$) [77].
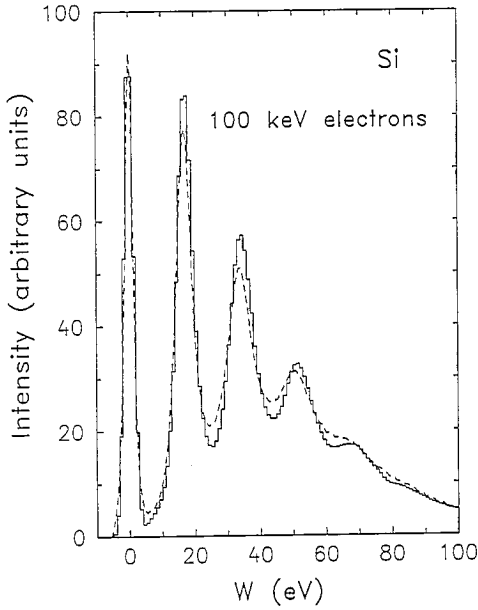
Fig. 7. Energy loss spectrum of 100 keV electrons transmitted through a thin silicon film. Dashed curve: spectrum as measured in our JEOL-100C electron microscope. The angular aperture is θ_{max} = 0.01 rad, and the energy resolution 3.2 eV FWHM. Histogram: LEEPS simulation result, assuming the same angular aperture and convoluted with a gaussian profile with the indicated FWHM. Experimental and simulated spectra are normalized to equal area. From our simulated results, the thickness of the sample is estimated to be 0.25±0.01 μm.
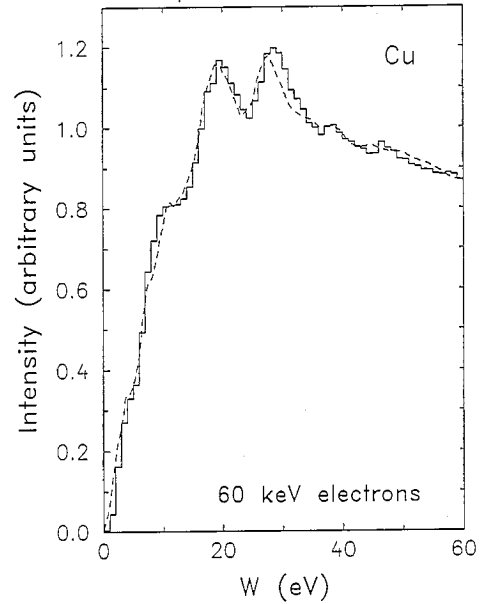
Fig. 8. Energy loss spectrum of 60 keV electrons transmitted through a thin copper film. Dashed curve: spectrum as measured by Misell and Atkins [82]. The angular aperture of their spectrometer was 0.1 rad, and its energy resolution was 1 eV FWHM. Histogram: LEEPS simulation result, assuming the same angular aperture and convoluted with a gaussian profile with the indicated FWHM. Experimental and simulated spectra are normalized to equal area. Optimal agreement with experiment is obtained with a film thickness of 0.10±0.01 μm.

scope (STEM) equipped with a LaB$_6$ filament in convergent beam coupled mode [81]. The transmitted beam was analyzed with a double focusing magnetic sector and the spectrum was detected by a YAG scintillator optically coupled to a Reticon 512 photo diode array. For the present comparison with simulation, we have assumed a simple gaussian energy resolution profile and estimated the energy calibration from the peak positions. Improved agreement may be obtained by simultaneously adjusting the spectrometer profile and the calibration. However, at present we rather wish to stress the fact that agreement with the experimental data is essentially obtained by using a detailed OOS density (see Eq. (18)). Also, the actual algorithm used to extend the OOS into the GOS is here of less importance. For the simulation of the characteristic energy loss spectra, optical-data models seem to be very useful and apparently superior to previous approaches.

Fig. 8 shows a similar comparison with experimental data from Misell and Atkins [82] for the case of copper. As in the previous case of silicon, the thickness of the film was not accurately known. Misell and Atkins quote their film thickness to be in the range 0.025–0.070 μm. We obtain good agreement between simulated and experimental data with a copper film thickness of 0.10±0.01 μm. It may be argued that the difference may indicate an error (then at least about 30%) in the inelastic mean free path calculated by LEEPS. However, comparing LEEPS with previous calculations by Tung et al. [59] and Ashley [18], this is highly unlikely. We

believe that the error may be at most about 10%, and more likely just a few percent. It should be noted that our OOS density for copper, using Eq. (18), is in very good agreement with the single collision energy loss spectrum derived by Misell and Atkins from their experimental data [19].

Appendix A: Exchange and relativistic corrections

We will briefly indicate the corrections of the inelastic scattering models which are made for relativistic effects and for exchange (when the incident particle is an electron). The relativistic corrections are necessary in order to get a sufficient accuracy at energies above ~ 50 keV and the exchange corrections cannot be neglected at any energy. Elastic scattering is, as mentioned, calculated entirely relativistically, being based on the Dirac equation, with a local exchange potential added for the case of electron scattering.

The complete formulae for the δ-oscillator and the TM model one-electron DCSs, including these corrections and with expressions for the mean free path and stopping power derived for the various contributions (resonance, binary, plasmon, etc.), are too long to be written here, but are summarized in Refs. [23,24].

We first consider exchange without relativistic corrections. Exchange in the inelastic scattering of electrons is taken approximately into account by means of a modified Born–Ochkur approximation [19]. The exchange-corrected

δ-oscillator DCS is

$$\left[\frac{d^2\sigma_\delta}{dQdW}\right]_{ex} = \frac{d^2\sigma_\delta}{dQdW}\,C_{ex}, \tag{A.1}$$

where $d^2\sigma_\delta/(dQdW)$ in the right member is the uncorrected DCS and

$$C_{ex} = 1 - \frac{Q}{E+W'-W} + \left(\frac{Q}{E+W'-W}\right)^2. \tag{A.2}$$

This reduces to the usual Born–Ochkur exchange correction [83] when $W = W'$, i.e. for distant (low-Q) collisions, and to the (non-relativistic) Møller DCS for electron-electron collisions when $Q = W$ and $W \gg W'$. The same correction factor C_{ex} is introduced in the TM model one-electron DCS $d^2\sigma_{TM}/(dQdW)$ for the inelastic scattering of electrons in a free-electron gas, but only for the electron–hole excitations. For the plasmon branch, we assume $C_{ex} = 1$. Note that $W' = 0$, so for momentum transfers beyond the plasmon cutoff ($Q > Q_c$), the usual Møller DCS is obtained exactly. It should also be observed that the integration limits are modified by the exchange effect; the details are described in Refs. [23,24].

We next consider relativistic corrections for electrons. We have here previously defined E as the non-relativistic kinetic energy, i.e. $E = mv^2/2$. We now redefine E to be the relativistic kinetic energy of the particle. Following Fano [84], the relativistic recoil energy is then conveniently defined by

$$Q\left(Q + 2mc^2\right) = (cq)^2, \tag{A.3}$$

so that the Bethe ridge will lie along the line $W = Q$ as in the non-relativistic case. Explicitly,

$$Q = \Big[E\left(E+2mc^2\right) + (E-W)\left(E-W+2mc^2\right)$$
$$\quad - 2\sqrt{E\left(E+2mc^2\right)}\sqrt{(E-W)\left(E-W+2mc^2\right)}$$
$$\quad \times \cos\theta + m^2c^4\Big]^{1/2} - mc^2. \tag{A.4}$$

As may be seen by comparing with Eq. (4), this gives a further modification of the integration limits [23,24].

For particles with kinetic energy less than ~ 0.5 MeV, the dominant relativistic effects on the DCS for low-Q excitations are purely kinematical; transverse interactions, and the associated density effect, can be neglected at these energies. The relativistic DCS for low-Q excitations, including the exchange correction, is given by [24]

$$\frac{d^2\sigma}{dQdW} = \frac{2\pi e^4}{mc^2\beta^2}\frac{1}{WQ}\frac{df(Q,W)}{dW}C_{ex}\left[1 - \mathcal{O}\left(\frac{Q}{2mc^2}\right)\right], \tag{A.5}$$

where

$$\beta^2 = \left(\frac{v}{c}\right)^2 = \frac{E(E+2mc^2)}{(E+mc^2)^2}. \tag{A.6}$$

For $Q \ll 2mc^2$ this is identical to the non-relativistic DCS, Eq. (6), which, written as in Eq. (A.5), therefore turns out to be sufficiently accurate for the low-Q excitations of electrons up to initial energies ~ 100 keV.

For the high-Q excitations we have to consider what happens on the Bethe ridge $Q = W$, i.e. for $W > W'$ in the δ-oscillator and for $W > Q_c$ in the TM model. For the scattering of electrons, we use here a modified Møller DCS [24,23]

$$\frac{d\sigma}{dW} = \frac{2\pi e^4}{mc^2\beta^2}\frac{1}{W^2}\left[1 + \left(\frac{W}{E+W'-W}\right)^2\right.$$
$$\quad \left. - \frac{(1-a)W}{E+W'-W} + \frac{aW^2}{(E+W')^2}\right], \tag{A.7}$$

where

$$a = \left(\frac{E}{E+mc^2}\right)^2. \tag{A.8}$$

Note that in the TM model $W' = 0$ and Eq. (A.7) reduces to the usual Møller DCS.

In LEEPS, positron inelastic scattering differs from electron inelastic scattering in the following respects [23]: $C_{ex} = 1$ everywhere, the integration limits are not modified by exchange effects, and the (modified) Møller DCS at high-Q collisions is replaced by the Bhabha DCS, which describes the collision of a positron with a free electron initially at rest. We do not take annihilation in flight into account.

Appendix B: Optical data preparation

One may start from the refractive index n and the extinction coefficient κ in the infrared, visible, ultraviolet and lower X-ray regions. These are comprehensively tabulated (as functions of photon energy W') e.g. by Palik et al. [60,61] for a number of solids. The dielectric constant is then, for each frequency $\omega = W'/\hbar$, given by

$$\epsilon(\omega) = (n + i\kappa)^2. \tag{B.1}$$

From this one obtains $\mathrm{Im}(-1/\epsilon(\omega))$, which is easily converted into the condensed matter OOS density by using Eq. (10) with $Q = 0$.

In some cases, these data have to be complemented by data in the x-ray region, i.e. related to inner-shell ionization. For this one may use the tabulated photoelectric cross section σ_{ph} [62–64]. At these high frequencies one has $|\epsilon| = 1$, in which case the OOS density is simply obtained by the formula [85]

$$\frac{df(W')}{dW'} = \frac{mc}{2\pi^2 e^2\hbar^2}\sigma_{ph}. \tag{B.2}$$

Actually, the preparation of an OOS table for a particular solid is not quite trivial [19]. One has to extrapolate to high

frequencies, check that the sum rules and the mean ionization energy come out correctly, and generally check for and correct against inconsistencies in the primary data. Once this preparation has been made, one has however a convenient data set which is generally applicable to the inelastic scattering of charged particles in that solid. The optical data used for the present calculations have been discussed in more detail in Ref. [19].

References

[1] M.J. Berger, in: Methods in Computational Physics, vol. 1, eds. B. Alder, S. Fernbach and M. Rotenberg (Academic Press, New York, 1963) p. 135.
[2] M. Green, Proc. Phys. Soc. 82 (1963) 204.
[3] H.E. Bishop, Brit. J. Appl. Phys. 18 (1967) 703.
[4] A.J. Green and R.C.G. Leckey, J. Phys. D: Appl. Phys. 9 (1976) 2123.
[5] R. Shimizu, Y. Kataoka, T. Ikuta, T. Koshikawa and H. Hashimoto, J. Phys. D: Appl. Phys. 9 (1976) 101.
[6] M. Kotera, K. Murata and K. Nagami, J. Appl. Phys. 52 (1981) 997 and 52 (1981) 7403.
[7] A. Desalvo, A. Parisini and R. Rosa, J. Phys. D: Appl. Phys. 17 (1984) 2455.
[8] L. Reimer and B. Lödding, Scanning 6 (1984) 128.
[9] S. Valkealahti and R.M. Nieminen, Appl. Phys. A 35 (1984) 51.
[10] D. Liljequist, J. Appl. Phys. 57 (1985) 657.
[11] J.D. Martínez, R. Mayol and F. Salvat, J. Appl. Phys. 67 (1990) 2955.
[12] Section 4.5 in: P. Andreo, Phys. Med. Biol. 36 (1991) 861.
[13] G. Love, M.G.C. Cox and V.D. Scott, J. Phys. D: Appl. Phys. 10 (1977) 7.
[14] D. Liljequist, J. Phys. D: Appl. Phys. 11 (1978) 839.
[15] A. Spalek and O. Dragoun, J. Phys. G: Nucl. Part. Phys. 19 (1993) 2071.
[16] K.O. Jensen and A.B. Walker, Surf. Sci. 292 (1993) 83.
[17] D.R. Penn, Phys. Rev. B 35 (1987) 482.
[18] J.C. Ashley, J. Electron Spectrosc. Relat. Phenom. 50 (1990) 323.
[19] J.M. Fernández-Varea, R. Mayol, D. Liljequist and F. Salvat, J. Phys.: Condens. Matter 5 (1993) 3593.
[20] A. Akkerman, T. Boutboul, A. Breskin, R. Chechik and A. Gibrekhterman, J. Appl. Phys. 76 (1994) 4656.
[21] N. Öztürk and W. Williamson, Jr., J. Appl. Phys. 74 (1993) 4723.
[22] Z.-J. Ding and R. Shimizu, Surf. Sci. 197 (1988) 539.
[23] J.M. Fernández-Varea, D. Liljequist and F. Salvat, University of Stockholm Institute of Physics Report 94-03 (1994).
[24] J.M. Fernández-Varea, D. Liljequist, R. Mayol and F. Salvat, University of Stockholm Institute of Physics Report 92-06 (1992).
[25] S. Goudsmit and J.L. Saunderson, Phys. Rev. 57 (1940) 24.
[26] H.W. Lewis, Phys. Rev. 78 (1950) 526.
[27] G. Molière, Z. Naturforsch. 3a (1948) 78.
[28] J.M. Fernández-Varea, R. Mayol, J. Baró and F. Salvat, Nucl. Instr. and Meth. B 73 (1993) 447.

[29] D. Liljequist, F. Salvat, R. Mayol and J.D. Martínez, J. Appl. Phys. 65 (1989) 2431; erratum, J. Appl. Phys. 66 (1989) 2768.
[30] Z. Czyzewski, D. O'Neill, C.J. MacCallum, A. Romig and D.C. Joy, J. Appl. Phys. 68 (1990) 3066.
[31] H. Raith, Acta Cryst. A 24 (1968) 85.
[32] F. Salvat, J.D. Martínez, R. Mayol and J. Parellada, Phys. Rev. A 36 (1987) 467.
[33] F. Salvat and R. Mayol, Comput. Phys. Commun. 74 (1993) 358.
[34] A.F. Akkerman and G.Ya. Chernov, Sov. Phys. Tech. Phys. 23 (1978) 247.
[35] S. Ichimura and R. Shimizu, Surf. Sci. 112 (1981) 386.
[36] D. Liljequist, M. Ismail, F. Salvat, R. Mayol and J.D. Martínez, J. Appl. Phys. 68 (1990) 3061.
[37] L. Landau, J. Phys. (USSR) 8 (1944) 201.
[38] P.V. Vavilov, Sov. Phys. JETP 5 (1957) 749.
[39] H. Bethe, Ann. Physik 5 (1930) 325.
[40] M. Inokuti, Rev. Mod. Phys. 43 (1971) 297.
[41] U. Fano, Phys. Rev. 103 (1956) 1202.
[42] R.H. Ritchie, Nucl. Instr. and Meth. 198 (1982) 81.
[43] M. Gryzinski, Phys. Rev. 138 (1965) A336.
[44] C.J. Powell, Surf. Sci. 44 (1974) 29.
[45] F. Wooten, Optical Properties of Solids (Academic Press, New York, 1972).
[46] L.D. Landau and E.M. Lifshitz, Electrodynamics of Continuous Media (Pergamon, Oxford, 1960).
[47] J.M. Fernández-Varea, R. Mayol, F. Salvat and D. Liljequist, J. Phys.: Condens. Matter 4 (1992) 2879.
[48] D. Liljequist, J. Phys. D: Appl. Phys. 16 (1983) 1567.
[49] N. Bohr, K. Dan. Vidensk. Selsk. Mat.-Fys. Medd. 18 (1948) no. 8.
[50] W.W.M. Allison and J.H. Cobb, Ann. Rev. Nucl. Part. Sci. 30 (1980) 253.
[51] R. Mayol and F. Salvat, J. Phys. B: At. Mol. Opt. Phys. 23 (1990) 2117.
[52] F. Salvat and J.M. Fernández-Varea, Nucl. Instr. and Meth. B 63 (1992) 255.
[53] H. Bichsel, Scanning Microsc. Suppl. 4 (1990) 147.
[54] J. Lindhard, K. Dan. Vidensk. Selsk. Mat.-Fys. Medd. 28 (1954) no. 8.
[55] R.H. Ritchie and A. Howie, Phil. Mag. 36 (1977) 463.
[56] J.C. Ashley, J. Electron Spectrosc. Relat. Phenom. 28 (1982) 177.
[57] J.C. Ashley, J. Electron Spectrosc. Relat. Phenom. 46 (1988) 199.
[58] J.C. Ashley, J. Appl. Phys. 69 (1991) 674.
[59] C.J. Tung, J.C. Ashley and R.H. Ritchie, Surf. Sci. 81 (1979) 427.
[60] Handbook of Optical Constants of Solids, edited by E.D. Palik (Academic Press, New York, 1985).
[61] Handbook of Optical Constants of Solids II, edited by E.D. Palik (Academic Press, New York, 1991).
[62] B.L. Henke, P. Lee, T.J. Tanaka, R.L. Shimabukuro and B.K. Fujikawa, At. Data Nucl. Data Tables 27 (1982) 1.
[63] B.L. Henke, E.M. Gullikson and J.C. Davis, At. Data Nucl. Data Tables 54 (1993) 181.
[64] D.E. Cullen, M.H. Chen, J.H. Hubbell, S.T. Perkins, E.F. Plechaty, J.A. Rathkopf and J.H. Scofield, Lawrence Livermore National Laboratory UCRL-50400 vol. 6 (1989) parts A and B.
[65] P. Schattschneider, P. Pongratz and H. Hohenegger, Scanning Microsc. Suppl. 4 (1990) 35.
[66] Z.-J. Ding and R. Shimizu, Surf. Sci. 222 (1989) 313.
[67] L. Reimer and H. Drescher, J. Phys. D: Appl. Phys. 10 (1977) 805.
[68] G. Neubert and S. Rogaschewski, J. Phys. D: Appl. Phys. 17 (1984) 2439.
[69] E.H. Darlington, J. Phys. D: Appl. Phys. 8 (1975) 85.
[70] H. Drescher, L. Reimer and H. Seidel, Z. Angew. Phys. 29 (1970) 331.
[71] P.G. Coleman, L. Albrecht, K.O. Jensen and A.B. Walker, J. Phys.: Condens. Matter 4 (1992) 10311.
[72] G.R. Massoumi, N. Hozhabri, W.N. Lennard and P.J. Schultz, Phys. Rev. B 44 (1991) 3486.
[73] J. Mäkinen, S. Palko, J. Martikainen and P. Hautojärvi, J. Phys.: Condens. Matter 4 (1992) L503.

[74] H.-J. Fitting, Phys. Stat. Sol. (a) 26 (1974) 525.

[75] J. Schou and H. Sørensen, J. Appl. Phys. 49 (1978) 816.

[76] H.-J. Hunger and L. Küchler, Phys. Stat. Sol. (a) 56 (1979) K45.

[77] G. Neubert and S. Rogaschewski, Phys. Stat. Sol. (a) 59 (1980) 35.

[78] R. Böngeler, U. Golla, M. Kässens, L. Reimer, B. Schindler, R. Senkel and M. Spranck, Scanning 15 (1993) 1.

[79] J. Baró, J. Sempau, J.M. Fernández-Varea and F. Salvat, Nucl. Instr. and Meth. B 100 (1995) 31.

[80] T. Matsukawa, R. Shimizu and H. Hashimoto, J. Phys. D: Appl. Phys. 7 (1974) 695.

[81] Z.W. Yuan, PhD Thesis (Stockholm University, 1993).

[82] D.L. Misell and A.J. Atkins, Phil. Mag. 27 (1973) 95.

[83] V.I. Ochkur, Sov. Phys. JETP 18 (1964) 503.

[84] U. Fano, Ann. Rev. Nucl. Sci. 13 (1963) 1.

[85] U. Fano and J.W. Cooper, Rev. Mod. Phys. 40 (1968) 441.